Geophysical Research Letters®

RESEARCH LETTER
10.1029/2024GL108631

Volcanic Precursor Revealed by Machine Learning Offers New Eruption Forecasting Capability

Kaiwen Wang[1], **Felix Waldhauser**[1], **Maya Tolstoy**[1,2], **David Schaff**[1], **Theresa Sawi**[1], **William S. D. Wilcock**[2], **and Yen Joe Tan**[3]

[1]Lamont-Doherty Earth Observatory, Columbia University, Palisades, NY, USA, [2]School of Oceanography, University of Washington, Seattle, WA, USA, [3]Department of Earth and Environmental Sciences, The Chinese University of Hong Kong, Hong Kong S.A.R., China

Key Points:

- Unsupervised learning separated regular earthquakes and precursory mixed frequency earthquakes (MFEs) based on different spectral patterns
- The regular earthquakes have strong tidal modulation, corresponding to failures on the caldera ring faults triggered by tidal stress changes
- The MFEs intensify 15 hr before eruption and migrate along pre-existing fissures, likely associated with eruption preparation processes

Supporting Information:

Supporting Information may be found in the online version of this article.

Correspondence to:

K. Wang,
kw2988@columbia.edu

Citation:

Wang, K., Waldhauser, F., Tolstoy, M., Schaff, D., Sawi, T., Wilcock, W. S. D., & Tan, Y. J. (2024). Volcanic precursor revealed by machine learning offers new eruption forecasting capability. *Geophysical Research Letters*, *51*, e2024GL108631. https://doi.org/10.1029/2024GL108631

Received 1 FEB 2024
Accepted 5 AUG 2024

Abstract Seismicity at active volcanoes provides crucial constraints on the dynamics of magma systems and complex fault activation processes preceding and during an eruption. We characterize time-dependent spectral features of volcanic earthquakes at Axial Seamount with unsupervised machine learning (ML) methods, revealing mixed frequency signals that rapidly increase in number about 15 hr before eruption onset. The events migrate along pre-existing fissures, suggesting that they represent brittle crack opening driven by influx of magma or volatiles. These results demonstrate the power of unsupervised ML algorithms to characterize subtle changes in magmatic processes associated with eruption preparation, offering new possibilities for forecasting Axial's anticipated next eruption. This analysis is generalizable and can be employed to identify similar precursory signals at other active volcanoes.

Plain Language Summary Our research used observations of small earthquakes to understand the dynamic behaviors of magma and fault systems before and during a volcano eruption. Specifically, we used ML techniques to search for patterns in the waveforms that may inform us of their associated physical processes. At Axial Seamount, an active underwater volcano, we discovered distinct patterns in earthquake signals preceding and during the 2015 eruption. Based on event spectral patterns, we identified signals of mixed-frequency earthquakes that rapidly increase in number about 15 hr before the eruption starts and migrate along pre-existing eruptive fissures. The spectral pattern involves a mixture of low frequency energy following the first arrivals, which we interpret to represent opening of cracks and being filled with magma or gases. Our study demonstrates that we can use ML algorithms to detect subtle changes in volcanic signals and help us better understand the processes leading up to an eruption. This may help us in forecasting Axial's upcoming eruption and can be applied to other active volcanoes too.

1. Introduction

Seismic observations can provide important constraints on the structure of a volcano and its dynamic behavior in volcanic cycles (Benz et al., 1996; Gudmundsson et al., 2016; Tan et al., 2019; Thurber, 1987; Wilcock et al., 2016; Wilding et al., 2023). Questions remain on how magma moves in the subsurface preceding an eruption and how soon before an eruption this process begins. Recent advances in unsupervised machine learning (ML) methods (Cotton & Ellis, 2011; Holtzman et al., 2018, 2021; Jenkins et al., 2021; Sawi et al., 2022; Seydoux et al., 2020; Yoon et al., 2015) offer the opportunity to mine large waveform archives to find subtle differences in the spectral content of seismic signals. These differences can be interpreted with respect to changes in source characteristics and the volcano-tectonic processes that drive brittle failure, providing a time-dependent image of physical processes that lead up to an eruption.

Axial Seamount is a well-instrumented, active submarine volcano on the Juan de Fuca Ridge (Figure 1) with a long record of geophysical data that covers the last three eruptions in 1998, 2011, and 2015 (Nooner & Chadwick, 2016; Wilcock et al., 2016, 2018), including documentation of the eruptive fissures and lava flows of the recent 2015 eruption (Chadwick et al., 2016), and 3-D images of its shallow magma chamber (Arnulf et al., 2014). Beginning five months before the most recent eruption in April 2015, seismicity at Axial Seamount has been recorded by a local, cabled, 7-station ocean bottom seismometer (OBS) network operated in real-time by the Ocean Observatories Initiative (OOI) (Kelley et al., 2014). The OBS array records signals from a variety of sources generated in both the solid Earth and the ocean (Wilcock et al., 2016), making the detection and identification of earthquakes difficult. Here we combine supervised and unsupervised ML methods to discriminate

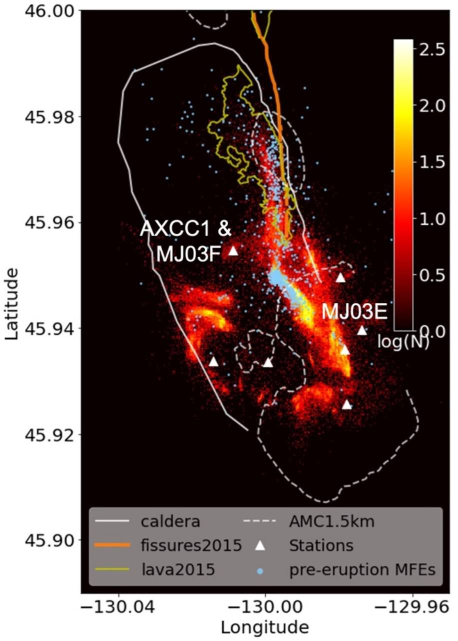

Figure 1. Heatmap of earthquake density at Axial Seamount from Nov 2014 to Dec 2021. Mixed-frequency earthquakes (MFEs) one day before the eruption are shown as light blue dots. Also shown are the caldera rim (white solid line), the 1.5 km depth contour of the Axial magma chamber (AMC) (dashed white line), eruptive fissures (orange lines), and lava flows (yellow lines) of the 2015 eruption and the OBS array (white triangles). The heatmap shows the number of earthquakes in each bin (bin size 25 m × 25 m). Locations of OBS station AXCC1 and two Bottom Pressure Recorders MJ03E and MJ03F are marked on the map. Earthquake catalog from Wang, Waldhauser, Schaff, Tolstoy, et al. (2024).

between earthquakes and other sources, and analyze spectral variation in earthquake signals in the 4 months leading up to the 2015 eruption. We find precursory signals with characteristic spectral patterns which we interpret as representing the movement of magma or volatiles during eruption preparation.

2. Unsupervised ML for Event Discrimination

We use the earthquake catalog of Wang, Waldhauser, Schaff, Tolstoy, et al. (2024) which was derived by combining supervised ML techniques (Zhu & Beroza, 2019; Zhu et al., 2022) with cross-correlation-based double-difference methods (Waldhauser & Ellsworth, 2000; Waldhauser et al., 2020) and a 3D velocity model (Baillard et al., 2019; Lomax et al., 2000). The catalog includes 240,000 earthquakes ($M = -1.74$ to 3.45) for Axial Seamount from 2014 to 2021 (Wang, Waldhauser, Schaff, Tolstoy, et al., 2024) that illuminate the caldera ring faults and the fissures that were active during the 2015 eruptions (Figure 1) (Waldhauser et al., 2020; Wilcock et al., 2016).

We apply an unsupervised ML method (SpecUFEx, Holtzman et al., 2018) to the 4 months of pre-eruption data (67,767 earthquakes recorded at station AXCC1 (Figure 1)) to characterize spectral patterns in the waveforms. SpecUFEx is an unsupervised spectral feature extraction algorithm originally developed using ML methods for audio pattern recognition (Cotton & Ellis, 2011) and has been adapted to characterize seismic waveforms of earthquakes (Holtzman et al., 2018), acoustic emissions (Holtzman et al., 2021), icequakes (Sawi et al., 2022), and repeating earthquakes (Sawi et al., 2023). It takes event spectrograms as input and applies nonnegative matrix factorization (NMF) and hidden Markov models (HMM) to reduce the dimensionality of the spectral features and remove features that are common to all signals.

For each earthquake in the 4 months of activity leading up to the eruption on 24 April 2015, we calculate a fingerprint matrix by counting the number of state transitions in the state sequence matrix from the HMM output. The fingerprints are condensed representations of the original earthquake spectrograms while still keeping their time-dependent spectral information. We further compress the fingerprints by principal component analysis (PCA) and finally apply K-means clustering to identify earthquake clusters that share common spectral features (Holtzman et al., 2018). We use waveform data from broadband OBS station AXCC1 and learned the feature dictionary from a representative subset of ~9,000 events in the week before the eruption. We then use the feature dictionary to calculate features of the ~4 months of seismicity starting from the beginning of 2015 until the eruption onset.

3. Clustering of Spectral Fingerprints

K-means clustering of the fingerprints separates the events into two main groups with small but distinct differences in spectral features in the waveforms between the groups (Figures 2a and 2d). To investigate which characteristic spectral features might contribute to the separation of the two earthquake clusters, we examine the representative patterns of the condensed fingerprints. By stacking the top 100 representative fingerprints in each cluster (Figures 2b and 2e), we identify the active states (bright spots in stacked fingerprints). These active states are the characteristic features that define the spectral feature space. We project these characteristic features in the fingerprints back onto the HMM and NMF mappings (emissions matrix in Figure S2A in Supporting Information S1 and spectral dictionary in Figure S2B in Supporting Information S1) to solve for their frequency-dependent sensitivity kernel (Figure S2C in Supporting Information S1). Comparing the frequency dependency of the characteristic features in the two clusters, we find that one cluster has events with a lower frequency wavetrain coming in shortly after the direct arrivals. We call the earthquakes in this cluster mixed-frequency earthquakes (MFEs) and the events in the other cluster regular earthquakes (EQs). The spectral

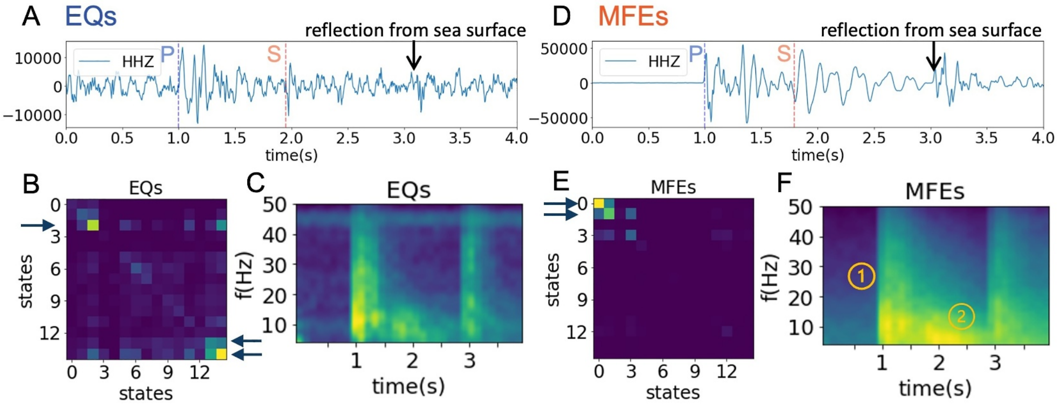

Figure 2. Spectral characteristics of events in the two main clusters. Waveform examples of one representative event in each cluster (a and d), stacked fingerprints (b and e), and stacked spectrograms (c and f) using 100 events in each cluster. P- and S-arrivals and reflections in the water column are marked. The water depth is ∼1.5 km so the reflections between the seafloor and the sea surface arrive ∼ 2 s after the direct seismic arrival. More waveform examples on three components are shown in supplementary Figure S7 in Supporting Information S1. The stacked fingerprints and stacked spectrograms are color scaled by their maximum value. Blue arrows in B and E point to the characteristic states of EQs and MFEs (Figure S2 in Supporting Information S1). ① and ② in F mark the impulsive P arrival and the low-frequency tail.

differences can also be seen in the stacked spectrograms (Figures 2c and 2f) of the top 100 representative events and their waveforms (Figures 2a and 2d).

4. Spatio-Temporal Distribution of MFEs

The separation based on spectral characteristics reveals differences in the spatiotemporal evolution of the earthquakes in the two groups (Figure 3, Movies S1 and S2). Approximately 24 hr prior to the eruption, the MFEs begin to occur on the eastern margin of the caldera along the southern segment of the eruptive fissures (Figure 1). These MFEs locate close to the roof of the Axial magma chamber (∼1.5 km; 15). ∼15 hr before the eruption, a distinct burst of MFEs migrates from the caldera center northward along the eastern margin of the caldera at a speed of 4.4 km/hr (arrow in Figure 3b). The peak hourly moment release of the MFEs during that burst is about two orders of magnitude above background, and 40 times that released by all regular earthquakes in the same period. After this initial burst, the MFEs activity subsides for a couple of hours and then, about 3.5 hr before the eruption, a second burst of MFEs occurred, reversing the path of the previous burst and migrating southward (at a speed of 1.1 km/hr) and eventually upward toward the location where the lava first erupted on the seafloor (Wilcock et al., 2016) (Figure 3b). After that point and for the next hour, the MFEs spread out across the entire fault system during the course of the eruption. The second MFE burst is characterized by a steep increase in seismic moment release starting about 4 hr and peaking 1 hr before the eruption onset. Peak hourly moment release is about 30 times that of the first burst, while the moment release from regular earthquakes leading up to the eruption is comparably insignificant. Once the eruption starts, MFEs moment release continuously decreases, while that from regular earthquakes increases. The MFEs rate remains low in the years following the eruption but they continue to comprise 10%–40% of the overall seismicity over time (Wang, Waldhauser, Schaff, Tolstoy, et al., 2024).

Different from the MFEs, the regular earthquakes locate primarily in the southern part of the caldera (Figure S4 in Supporting Information S1). They occur on both the eastern and western walls of the ring fault, which suggests that the spectral fingerprints are not sensitive to event location relative to the seismic station. The regular earthquake cluster also includes events during the pre-eruption inflation period as well as the rapid deflation period after the eruption started, that is, when the fault slip motion on the caldera ring faults reversed from normal faulting to thrust faulting (Wilcock et al., 2016). This suggests that the fingerprints are also not sensitive to the reversal of fault slip motion.

Tidal triggering of earthquakes is observed at Axial seamount, especially prior to the eruption (Scholz et al., 2019; Tan et al., 2019; Tolstoy et al., 2002; Wilcock et al., 2016). Here, we compare the temporal correlation between the two spectral clusters we identified and the ocean tide to understand their driving mechanisms. We find that the

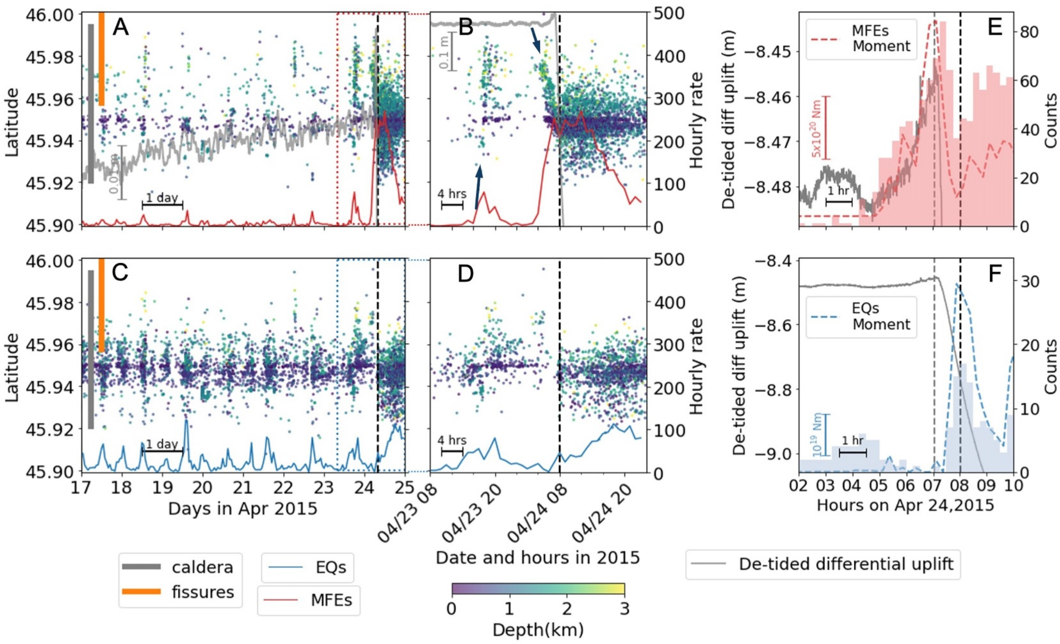

Figure 3. Pre-eruption temporal evolution of the two spectral clusters. The MFEs (top panels) and earthquakes (bottom panels) spatiotemporal distributions in ~1 week (a and c), ~2 days (b and d), and 8 hr (e and f) time scale. The top and bottom panels are plotted with the same time axis for MFEs (a, b, and e) and earthquakes (c, d, and f) activity. The red and blue curves (a–d) are hourly seismicity rates. Gray curves (a–f) show volcano inflation represented by detided differential uplift measurement between two bottom pressure recorders (BPRs) at sites MJ03E and MJ03F (Figure 1) (Chadwick et al., 2022). Dashed red and blue curves (e and f) show the binned seismic moment of the MFEs and earthquakes during the eruption. The dashed black vertical line (a–f) marks the time of eruption onset at 8:01 when the lava first reaches the seafloor (Wilcock et al., 2016). Arrows in panel (b) point to northward and southward migration of MFEs prior to the eruption. The dashed gray vertical line (e and f) marks the time of maximum inflation at 7:03 (e and f).

rate of regular earthquakes closely follows the tidal cycle over the observation period (Figure 3d, Figure S5 in Supporting Information S1). Given their locations and the temporal correlation with the tides, we infer that these earthquakes generally occur on critically stressed ring faults and are triggered by small stress changes. The MFE cluster, during the same period, shows rather sparsely distributed bursts of events (Figure S3A in Supporting Information S1) which mostly lie along the eastern edge of the caldera to the north (Figure S6 in Supporting Information S1). Among these bursts, we do not observe a clear migration pattern over long distances (Figure S6 in Supporting Information S1) as seen in the two very active bursts that relate to the north-south migration ~15 hr and ~3.5 hr before the eruption onset (Figure 3b). The timings of the MFE bursts correlate with the tides in many cases (Figure S3 in Supporting Information S1), but they locate further to the north compared with the tidal driven earthquakes (Figure 3). We do not observe any systematic offset between the timing of the MFE bursts and the peak of regular earthquakes. This suggests that the underlying driver for the two different types of earthquakes may be the same (e.g., magma pressure), or that the drivers respond to the tidal forcing in a similar way.

5. Discussion and Conclusion

Two possible explanations of the difference in spectral features between the MFE and EQ groups are path effect and source effect. Spatially variant attenuation patterns, especially in local complex volcanic structures, may cause differences in frequency content if observed along different paths. However, we find that the same clustering analysis carried out at other stations (AXAS1, AXEC2) in the OBS network gives similar groupings (Supplementary materials, Figure S1 in Supporting Information S1). If path effects were causing the clustering, we would expect different event groupings at stations that sample different source-receiver paths. It is also possible that attenuation or velocity changes occur in a region that is local to the source. However, we find that closely located and timed events from the two groups still show different spectral behavior at a common station. Therefore, we infer that the spectral difference between the two groups is likely caused by differences in the source mechanisms.

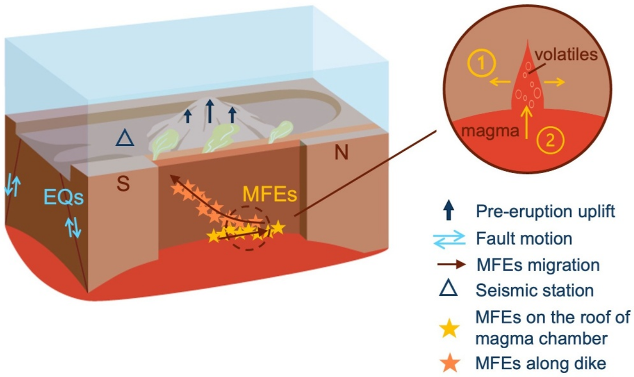

Figure 4. Cartoon summarizing observations. Tidal-driven earthquakes occur on caldera ring faults while the MFEs track movement of volatiles and magma prior to the eruption. Inset shows possible mechanisms of the MFEs. ① and ② correspond to the crack opening (brittle onset in Figure 2F) and volatile/magma influx (low-frequency tail in Figure 2F) processes.

There are many possibilities that can explain source differences, including differences in fault stress state, faulting mechanisms, or the effects of fluid. Wilcock et al. (2016) detected southward migration of pre-eruption seismicity along the east wall in the hours before the eruption and associated it with southward dike propagation and opening of eruptive fissures. It is possible that the MFEs are tracking magmatic processes associated with opening cracks and thus include non-double-couple components from the crack opening mode in contrast to simple shear failures of earthquakes on the ring faults (Foulger et al., 2004). In this process, the low-frequency content in the MFE waveforms might be generated by magma or volatiles filling the crack, as observed in studies at other volcanoes (Chouet & Matoza, 2013; Cui et al., 2021; Song et al., 2023; Woods et al., 2018).

When comparing the moment release of MFEs with available differential elevation data (Nooner & Chadwick, 2016) we find that the peak moment coincides with the peak in inflation about 1 hour before the eruption (gray curves in Figure 3e). Moment release for the earthquakes, on the other hand, is highest during the time of rapid deflation after lava erupted. This suggests the MFEs are associated with magmatic processes during the pre-eruption inflation process, while the regular earthquakes are triggered by the stress change on the ring faults as the magma chamber deflates. In the pre-eruption period, the MFEs in the north also correlate with the region of maximum uplift observed in deformation measurement (Nooner & Chadwick, 2016), illuminating the segment of the eruptive fissure where the following eruption started.

Given that the MFEs locate along the eruptive fissures near the roof of the magma chamber and the documented high CO2 content at Axial seamount (Dixon et al., 1988), the MFEs are likely caused by brittle crack opening and subsequent movement of magma and/or volatiles into the zones of weakness created by increasing magma pressure. In fact, the observation that they distribute widely in space and time suggests they are more likely related to CO2 release as opposed to magma movement. Because MFEs are detected for months prior to the eruption, it implies there is an extended period of magma intrusion or volatile release possibly associated with inflating sills. However, the behavior of early MFE bursts suggests that this magmatic process may also occur at smaller scale at depth with no clear migration pattern observable along the dike, consistent with the idea of the presence of volatiles. As the magma pressure builds up, the dike finally forms along the weakened zones and initiates the southward propagation, which is observed as intense MFE activity starting ~3.5 hr before the eruption. Figure 4 shows a cartoon summarizing the physical and magmatic processes and associated seismicity at Axial.

Short-term volcano eruption forecasting has long been a challenging task due to the lack of clear and reliable precursory signals. Common prediction metrics include long-term deformation measurement, changes in tidal triggering, and short-term seismicity increase (Barberi et al., 1992; Chouet, 1996; Chouet et al., 1994; Nooner & Chadwick, 2016; Wilcock et al., 2016, 2018). In this study, unsupervised ML revealed the rapid increase of a precursory signal defined as MFEs. These signals differ substantially from volcano-tectonic (VT; Lahr et al. (1994); Chouet et al. (1994)) or long-period (LP; Minakami (1974); Shimozuru and Kagiyama (1989); Chouet et al. (1994)) earthquakes or tremors (Chouet, 1996; Julian, 1994; Koyanagi et al., 1987; Shimozuru & Kamo, 1966), as they contain both short and long period waves. Although they may resemble some of the previously reported hybrid frequency earthquakes (HFE; Lahr et al. (1994); Harrington and Brodsky (2007); Yu et al. (2021); Coté et al. (2010); Cui et al. (2021)), our observations suggest that their mechanism might be different. Interpretations of previously observed hybrid earthquakes include path effects caused by strong attenuation or low-velocity layers, and source effects due to low stress drop, slow rupture speed, or fluid resonance. Our analysis indicates that the characteristic spectral features of the MFEs likely originate from source effects rather than path effects, making them a potential precursory signal to track volatile and/or magma movement during eruption preparation. This precursory MFE activity intensifies ~15 hr before the eruption and peaks ~1 hr before the magma reaches the seafloor, which offers an opportunity to improve short-term eruption forecasting on time scales of hours to days. With the capability to identify such precursory signals in real time (Wang, Waldhauser, Schaff, Tolstoy, et al., 2024), we can now monitor these signals as Axial is preparing for its next eruption predicted to occur within the 2025–2030 time period (Chadwick et al., 2022). More importantly, the novel use of unsupervised ML opens up a new opportunity to investigate whether such precursory seismic signals exist at other active volcanoes.

Data Availability Statement

Seismic waveforms used in this study were downloaded from the EarthScope Consortium Data Management Center (DMC) (https://ds.iris.edu/ds/nodes/dmc/data/) (Rutgers University, 2013). The earthquake catalog (Wang, Waldhauser, Schaff, Tolstoy, et al., 2024) is available on Figshare (https://doi.org/10.6084/m9.figshare.25130162.v1) (Wang, Waldhauser, & Schaff, 2024a). The earthquake catalog is also available at our Axial Seamount real-time monitoring website (https://axialdd.ldeo.columbia.edu) (Wang, Waldhauser, & Schaff, 2024b). The SpecUFEx package can be accessed at https://github.com/Specufex/specufex (Holtzman et al., 2024).

Acknowledgments
This work received support from NSF awards OAC-2103741 and OCE-1951448. We would like to thank reviewer Phil Dawson and editor Christian Huber for providing constructive comments and suggestions that helped improve the manuscript and Eric Beauce and Ben Holtzman for fruitful discussions.

References

Arnulf, A., Harding, A., Kent, G., Carbotte, S., Canales, J., & Nedimović, M. (2014). Anatomy of an active submarine volcano. *Geology*, *42*(8), 655–658. https://doi.org/10.1130/g35629.1

Baillard, C., Wilcock, W. S., Arnulf, A. F., Tolstoy, M., & Waldhauser, F. (2019). A joint inversion for three-dimensional P and S wave velocity structure and earthquake locations beneath axial seamount. *Journal of Geophysical Research: Solid Earth*, *124*(12), 12997–13020. https://doi.org/10.1029/2019jb017970

Barberi, F., Bertagnini, A., Landi, P., & Principe, C. (1992). A review on phreatic eruptions and their precursors. *Journal of Volcanology and Geothermal Research*, *52*(4), 231–246. https://doi.org/10.1016/0377-0273(92)90046-g

Benz, H., Chouet, B., Dawson, P., Lahr, J., Page, R., & Hole, J. (1996). Three-dimensional P and S wave velocity structure of redoubt volcano, Alaska. *Journal of Geophysical Research*, *101*(B4), 8111–8128. https://doi.org/10.1029/95jb03046

Chadwick, W., Paduan, J., Clague, D., Dreyer, B., Merle, S., Bobbitt, A., et al. (2016). Voluminous eruption from a zoned magma body after an increase in supply rate at Axial Seamount. *Geophysical Research Letters*, *43*(23), 12–063. https://doi.org/10.1002/2016gl071327

Chadwick, W., Wilcock, W. S., Nooner, S. L., Beeson, J. W., Sawyer, A. M., & Lau, T.-K. (2022). Geodetic monitoring at Axial Seamount since its 2015 eruption reveals a waning magma supply and tightly linked rates of deformation and seismicity. *Geochemistry, Geophysics, Geosystems*, *23*(1), e2021GC010153. https://doi.org/10.1029/2021gc010153

Chouet, B. A. (1996). Long-period volcano seismicity: Its source and use in eruption forecasting. *Nature*, *380*(6572), 309–316. https://doi.org/10.1038/380309a0

Chouet, B. A., & Matoza, R. S. (2013). A multi-decadal view of seismic methods for detecting precursors of magma movement and eruption. *Journal of Volcanology and Geothermal Research*, *252*, 108–175. https://doi.org/10.1016/j.jvolgeores.2012.11.013

Chouet, B. A., Page, R. A., Stephens, C. D., Lahr, J. C., & Power, J. A. (1994). Precursory swarms of long-period events at redoubt volcano (1989–1990), Alaska: Their origin and use as a forecasting tool. *Journal of Volcanology and Geothermal Research*, *62*(1–4), 95–135. https://doi.org/10.1016/0377-0273(94)90030-2

Coté, D. M., Belachew, M., Quillen, A. C., Ebinger, C. J., Keir, D., Ayele, A., & Wright, T. (2010). Low-frequency hybrid earthquakes near a magma chamber in Afar: Quantifying path effects. *Bulletin of the Seismological Society of America*, *100*(5A), 1892–1903. https://doi.org/10.1785/0120090111

Cotton, C. V., & Ellis, D. P. (2011). Spectral vs. spectro-temporal features for acoustic event detection. In *2011 IEEE workshop on applications of signal processing to audio and acoustics (waspaa)* (pp. 69–72).

Cui, X., Li, Z., & Huang, H. (2021). Subdivision of seismicity beneath the summit region of Kīlauea Volcano: Implications for the preparation process of the 2018 eruption. *Geophysical Research Letters*, *48*(20), e2021GL094698. https://doi.org/10.1029/2021gl094698

Dixon, J. E., Stolper, E., & Delaney, J. R. (1988). Infrared spectroscopic measurements of CO2 and H2O in Juan de Fuca Ridge basaltic glasses. *Earth and Planetary Science Letters*, *90*(1), 87–104. https://doi.org/10.1016/0012-821x(88)90114-8

Foulger, G., Julian, B., Hill, D., Pitt, A., Malin, P., & Shalev, E. (2004). Non-double-couple microearthquakes at Long Valley Caldera, California, provide evidence for hydraulic fracturing. *Journal of Volcanology and Geothermal Research*, *132*(1), 45–71. https://doi.org/10.1016/s0377-0273(03)00420-7

Gudmundsson, M. T., Jónsdóttir, K., Hooper, A., Holohan, E. P., Halldórsson, S. A., Ófeigsson, B. G., et al. (2016). Gradual caldera collapse at Bárdarbunga Volcano, Iceland, regulated by lateral magma outflow. *Science*, *353*(6296), aaf8988. https://doi.org/10.1126/science.aaf8988

Harrington, R. M., & Brodsky, E. E. (2007). Volcanic hybrid earthquakes that are brittle-failure events. *Geophysical Research Letters*, *34*(6). https://doi.org/10.1029/2006gl028714

Holtzman, B., Groebner, N., Sawi, T., Xing, T., Pec, M., Ghaffari, H., et al. (2021). Unsupervised spectral feature extraction applied to acoustic emissions during brittle creep of basalt under dry and wet conditions. In *Agu fall meeting abstracts* (Vol. 2021, pp. H12E-04).

Holtzman, B., Paté, A., Paisley, J., Waldhauser, F., & Repetto, D. (2018). Machine learning reveals cyclic changes in seismic source spectra in Geysers geothermal field. *Science Advances*, *4*(5), eaao2929. https://doi.org/10.1126/sciadv.aao2929

Holtzman, B., Sawi, T., & Groebner, N. (2024). Specufex github repository [Software]. https://github.com/Specufex/specufex

Jenkins, W. F., Gerstoft, P., Bianco, M. J., & Bromirski, P. D. (2021). Unsupervised deep clustering of seismic data: Monitoring the ross ice shelf, Antarctica. *Journal of Geophysical Research: Solid Earth*, *126*(9), e2021JB021716. https://doi.org/10.1029/2021jb021716

Julian, B. R. (1994). Volcanic tremor: Nonlinear excitation by fluid flow. *Journal of Geophysical Research*, *99*(B6), 11859–11877. https://doi.org/10.1029/93jb03129

Kelley, D. S., Delaney, J. R., & Juniper, S. K. (2014). Establishing a new era of submarine volcanic observatories: Cabling Axial Seamount and the Endeavour Segment of the Juan de Fuca Ridge. *Marine Geology*, *352*, 426–450. https://doi.org/10.1016/j.margeo.2014.03.010

Koyanagi, R. Y., Chouet, B., & Aki, K. (1987). Origin of volcanic tremor in Hawai‘i. *U. S. Geological Survey Professional Paper*, *1350*(2), 1221–1257.

Lahr, J. C., Chouet, B. A., Stephens, C. D., Power, J. A., & Page, R. A. (1994). Earthquake classification, location, and error analysis in a volcanic environment: Implications for the magmatic system of the 1989–1990 eruptions at Redoubt Volcano, Alaska. *Journal of Volcanology and Geothermal Research*, *62*(1–4), 137–151. https://doi.org/10.1016/0377-0273(94)90031-0

Lomax, A., Virieux, J., Volant, P., & Berge-Thierry, C. (2000). Probabilistic earthquake location in 3D and layered models: Introduction of a Metropolis-Gibbs method and comparison with linear locations. *Advances in seismic event location*, 101–134.

Minakami, T. (1974). Seismology of volcanoes in Japan. In *Developments in solid earth geophysics* (Vol. 6, pp. 1–27). Elsevier. https://doi.org/10.1016/b978-0-444-41141-9.50007-3

Nooner, S. L., & Chadwick, W. (2016). Inflation-predictable behavior and co-eruption deformation at Axial Seamount. *Science*, *354*(6318), 1399–1403. https://doi.org/10.1126/science.aah4666

Rutgers University. (2013). Ocean observatories initiative. [Dataset]. *International Federation of Digital Seismograph Networks*. https://doi.org/10.7914/SN/OO

Sawi, T., Holtzman, B., Walter, F., & Paisley, J. (2022). An unsupervised machine-learning approach to understanding seismicity at an Alpine Glacier. *Journal of Geophysical Research: Earth Surface*, *127*(12), e2022JF006909. https://doi.org/10.1029/2022jf006909

Sawi, T., Waldhauser, F., Holtzman, B. K., & Groebner, N. (2023). Detecting repeating earthquakes on the San Andreas Fault with unsupervised machine learning of spectrograms. *The Seismic Record*, *3*(4), 376–384. https://doi.org/10.1785/0320230033

Scholz, C. H., Tan, Y. J., & Albino, F. (2019). The mechanism of tidal triggering of earthquakes at mid-ocean ridges. *Nature Communications*, *10*(1), 2526. https://doi.org/10.1038/s41467-019-10605-2

Seydoux, L., Balestriero, R., Poli, P., Hoop, M. d., Campillo, M., & Baraniuk, R. (2020). Clustering earthquake signals and background noises in continuous seismic data with unsupervised deep learning. *Nature Communications*, *11*(1), 3972. https://doi.org/10.1038/s41467-020-17841-x

Shimozuru, D., & Kagiyama, T. (1989). Some significant features of pre-eruption volcanic earthquakes. In *Volcanic hazards: Assessment and monitoring* (pp. 504–512).

Shimozuru, D., & Kamo, K. (1966). Volcanic tremor of Kīlauea volcano, Hawai'i, during July-December, 1963.

Song, Z., Tan, Y. J., & Roman, D. C. (2023). Deep long-period earthquakes at Akutan Volcano from 2005 to 2017 better track magma influxes compared to volcano-tectonic earthquakes. *Geophysical Research Letters*, *50*(10), e2022GL101987. https://doi.org/10.1029/2022gl101987

Tan, Y. J., Waldhauser, F., Tolstoy, M., & Wilcock, W. S. (2019). Axial seamount: Periodic tidal loading reveals stress dependence of the earthquake size distribution (b value). *Earth and Planetary Science Letters*, *512*, 39–45. https://doi.org/10.1016/j.epsl.2019.01.047

Thurber, C. H. (1987). Seismic structure and tectonics of Kīlauea Volcano. *U. S. Geological Survey Professional Paper*, *1350*(2), 919–934.

Tolstoy, M., Vernon, F. L., Orcutt, J. A., & Wyatt, F. K. (2002). Breathing of the seafloor: Tidal correlations of seismicity at Axial Volcano. *Geology*, *30*(6), 503–506. https://doi.org/10.1130/0091-7613(2002)030<0503:botstc>2.0.co;2

Waldhauser, F., & Ellsworth, W. L. (2000). A double-difference earthquake location algorithm: Method and application to the northern Hayward fault, California. *Bulletin of the Seismological Society of America*, *90*(6), 1353–1368. https://doi.org/10.1785/0120000006

Waldhauser, F., Wilcock, W., Tolstoy, M., Baillard, C., Tan, Y., & Schaff, D. (2020). Precision seismic monitoring and analysis at Axial Seamount using a real-time double-difference system. *Journal of Geophysical Research: Solid Earth*, *125*(5), e2019JB018796. https://doi.org/10.1029/2019jb018796

Wang, K., Waldhauser, F., & Schaff, D. P. (2024a). Axial catalog [Dataset]. *Figshare*. https://doi.org/10.6084/m9.figshare.25130162.v1

Wang, K., Waldhauser, F., & Schaff, D. P. (2024b). Real-time, high-precision, deep magnitude earthquake catalog for axial seamount. [Dataset]. https://axialdd.ldeo.columbia.edu

Wang, K., Waldhauser, F., Schaff, D. P., Tolstoy, M., Wilcock, W. S. D., & Tan, Y. J. (2024). Real-time detection of volcanic unrest and eruption at Axial Seamount using machine learning. *Seismological Research Letters*. https://doi.org/10.1785/0220240086

Wilcock, W. S., Dziak, R. P., Tolstoy, M., Chadwick Jr, W. W., Nooner, S. L., Bohnenstiehl, D. R., et al. (2018). The recent volcanic history of Axial Seamount: Geophysical insights into past eruption dynamics with an eye toward enhanced observations of future eruptions. *Oceanography*, *31*(1), 114–123. https://doi.org/10.5670/oceanog.2018.117

Wilcock, W. S., Tolstoy, M., Waldhauser, F., Garcia, C., Tan, Y. J., Bohnenstiehl, D. R., et al. (2016). Seismic constraints on caldera dynamics from the 2015 Axial Seamount eruption. *Science*, *354*(6318), 1395–1399. https://doi.org/10.1126/science.aah5563

Wilding, J. D., Zhu, W., Ross, Z. E., & Jackson, J. M. (2023). The magmatic web beneath Hawai'i. *Science*, *379*(6631), 462–468. https://doi.org/10.1126/science.ade5755

Woods, J., Donaldson, C., White, R. S., Caudron, C., Brandsdóttir, B., Hudson, T. S., & Ágústsdóttir, T. (2018). Long-period seismicity reveals magma pathways above a laterally propagating dyke during the 2014–15 Bároarbunga rifting event, Iceland. *Earth and Planetary Science Letters*, *490*, 216–229. https://doi.org/10.1016/j.epsl.2018.03.020

Yoon, C. E., O'Reilly, O., Bergen, K. J., & Beroza, G. C. (2015). Earthquake detection through computationally efficient similarity search. *Science Advances*, *1*(11), e1501057. https://doi.org/10.1126/sciadv.1501057

Yu, H., Harrington, R. M., Kao, H., Liu, Y., & Wang, B. (2021). Fluid-injection-induced earthquakes characterized by hybrid-frequency waveforms manifest the transition from aseismic to seismic slip. *Nature Communications*, *12*(1), 6862. https://doi.org/10.1038/s41467-021-26961-x

Zhu, W., & Beroza, G. C. (2019). Phasenet: A deep-neural-network-based seismic arrival-time picking method. *Geophysical Journal International*, *216*(1), 261–273.

Zhu, W., McBrearty, I. W., Mousavi, S. M., Ellsworth, W. L., & Beroza, G. C. (2022). Earthquake phase association using a Bayesian Gaussian mixture model. *Journal of Geophysical Research: Solid Earth*, *127*(5), e2021JB023249. https://doi.org/10.1029/2021jb023249